New Journal of Physics
The open-access journal for physics

Spin-detection in a quantum electromechanical shuttle system

J Twamley[1,5], D W Utami[2], H-S Goan[3] and G Milburn[4]

[1] Centre for Quantum Computer Technology, Macquarie University, Sydney, NSW 2109, Australia
[2] School of Physical Sciences, University of Queensland, St Lucia, QLD 4072, Australia
[3] Department of Physics, National Taiwan University, Taipei 106, Taiwan, Republic of China
[4] Centre for Quantum Computer Technology, The University of Queensland, St Lucia, QLD 4072, Australia
E-mail: jtwamley@ics.mq.edu.au

New Journal of Physics **8** (2006) 63
Received 5 December 2005
Published 2 May 2006
Online at http://www.njp.org/
doi:10.1088/1367-2630/8/5/063

Abstract. We study the electrical transport of a harmonically bound, single-molecule C_{60} shuttle operating in the Coulomb blockade regime, i.e. single electron shuttling. In particular, we examine the dependance of the tunnel current on an ultra-small stationary force exerted on the shuttle. As an example, we consider the force exerted on an endohedral $N@C_{60}$ by the magnetic field gradient generated by a nearby nanomagnet. We derive a Hamiltonian for the full shuttle system which includes the metallic contacts, the spatially dependent tunnel couplings to the shuttle, the electronic and motional degrees of freedom of the shuttle itself and a coupling of the shuttle's motion to a phonon bath. We analyse the resulting quantum master equation and find that, due to the exponential dependence of the tunnel probability on the shuttle-contact separation, the current is highly sensitive to very small forces. In particular, we predict that the spin state of the endohedral electrons of $N@C_{60}$ in a large magnetic gradient field can be distinguished from the resulting current signals within a few tens of nanoseconds. This effect could prove useful for the detection of the endohedral spin-state of individual paramagnetic molecules such as $N@C_{60}$ and $P@C_{60}$, or the detection of very small static forces acting on a C_{60} shuttle.

[5] Author to whom any correspondence should be addressed.

PII: S1367-2630(06)13829-X

Contents

1. Introduction

The determination of the spin-state of a single electron spin has attracted much attention recently [1]–[3]. Following the discussion by Gorelik *et al* of a charge shuttle [4] consisting of a small movable grain (mechanical degrees of freedom) coupled via tunnel barriers to source and drain electrodes, interest in such or similar electromechanical systems has blossomed [5]–[20] and several elegant experiments [21]–[26] toward their realizations have been reported. Some of the investigations have focused on the quantum aspects of the electromechanical system where the mechanical motion is quantized [27]–[39]. They are also called the quantum electromechanical systems (QEMSs). The experiments of Park *et al* in the observation of quantized mechanical motional transitions in the conductance of a single-molecule C_{60} transistor [21], is particularly interesting in the context of our discussion below. In this work, we wish to examine whether a QEMS, with the inclusion of spin degrees of freedom, or a Spin–QEMS, can be used to detect the spin-state of the included spin. We have in mind the particular case of nitrogen or phosphorous endohedrally doped C_{60}, $N@C_{60}$ or $P@C_{60}$. This material has previously been shown to possess unpaired endohedrally trapped electrons, in a quartet ground state, $S = 3/2$, and which display exceedingly long transverse relaxation (or T_2), times. This material has been considered for use in quantum information processing devices but may have uses in other areas related to classical spintronic memories.

As a first exploration, one can consider the original experiment of Park *et al* using the paramagnetic endohedral, like $P@C_{60}$, instead of C_{60}. It is known that the electronic spin degrees of freedom reside in the endohedral electrons which are concentrated isotropically at the centre of the C_{60} cage in $P@C_{60}$ [40]. In the experiment of [21], the C_{60} oscillates in a Harmonic potential at THz frequencies. For the Spin–QEMS system of a $P@C_{60}$ molecule as a movable

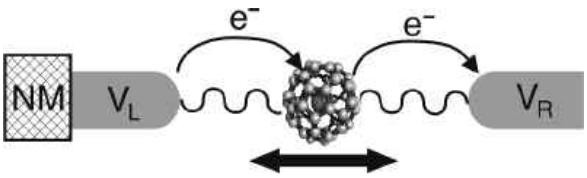

Figure 1. Pictorial representation of the proposed shuttle device similar to [4], where the N@C_{60} molecular shuttle is held harmonically (e.g. by organic ligands), between two conducting electrodes. NM labels a nearby (<10 nm) nanomagnet (similar to those found in current Magnetic Force Microscopes), which provides a large magnetic field gradient thus yielding a spin-dependant force on the shuttle via the interaction of the endohedral spin contained in N@C_{60} and the magnetic gradient field. The left and right tunnel contacts are held at the voltages V_L and V_R respectively.

island in a single molecule transistor, one must be capable of engineering a coupling between the state of the endohedral spin and the conductance properties of the transistor. This can be accomplished through the imposition of a large magnetic field gradient $\partial B/\partial x$, along the plane of the transistor. The interaction between the endohedral spin and this gradient field will impart a small force on the molecule which will in turn, cause a slight shift in the equilibrium position within the damped Harmonic oscillator trapping potential, shifting the molecule towards one of the contacts. This small shift will lead to a change in conductance properties. It will be shown that if the configuration is asymmetric, i.e. the mobile island is closer to one lead than the other, the resulting current depends *exponentially*, on this small spatial displacement. In the case of a tight trapping, observed in Park *et al* [21], the resulting spin-dependent change in conductance is extremely small and unobservable. If we instead configure for the largest achievable magnetic field gradient (obtained for instance in Magnetic Resonance Force Microscopy (MRFM) devices), by placing a nanoscopic permanent magnet near to the mobile island, we also find that due to the large difference between the energy scales of the endohedral electronic spin flip (GHz), and the island's Harmonic motion in [21], (THz), the island's spin-dependent position shift is minute and is unobservable in the current.

Guided by these observations, we instead consider the more 'floppy' Spin–QEMS of a shuttle device where the restoring oscillator now operates in the GHz frequency regime (see figure 1). MRFM cantilevers fabricated out of single Si crystals have recently been generated which have resonant frequencies in the GHz range [41]. The resulting device could be similar to that outlined by Isacsson [5]. It may also be possible to engineer non-conducting flexible linker molecules which will connect the shuttle molecule to the metallic contacts and have resonant frequencies in the GHz range.

We thus consider the system of a movable shuttle or island, which is harmonically bound to oscillate between two metallic contacts in the presence of significant motional damping. We further assume that we operate in the Coulomb blockade region where only one electron can reside on the shuttle at one time. For the particular case of an endohedral N{P}@C_{60} island, as in [42], we make the assumption that this injected electron distributes itself isotropically around the surface of the C_{60} cage thus averaging out any magnetic dipole coupling between the spin state of the injected electron and the spin state of the endohedral electrons. We also assume

that the injected electrons are not spin polarized and the resulting force experienced by the shuttle due to the interaction between the spin of the injected electrons and the magnetic gradient will average out while the force on the shuttle due to the endohedral electrons interacting with the magnetic field remains static. We therefore neglect the random spin-force contribution of the injected electrons in what follows. Recently, spin-dependent transport properties in slightly different setups of the nano-electromechanical systems coupled to spin-polarized electrodes have been investigated [43]–[47].

Before going into the model in detail, we can understand, in a simple but surprisingly robust manner, the underlying reasons why we expect to achieve an *exponential* dependence of the current on the island's displacement from its equilibrium position. The current through a simple source-fixed island-drain, two-stage sequential tunnelling process [48, 49], in terms of the left and right tunnel rates γ_L, γ_R, is given by

$$i \sim \frac{\gamma_L \gamma_R}{\gamma_R + \gamma_L}. \tag{1}$$

If we now take into account the exponential dependence of these tunnel rates on the position of the (now mobile) island, and letting δ (positive) be the small displacements of the island from its equilibrium position to the right (to the drain), we can set

$$\gamma_L \sim \gamma_L^0 e^{-\lambda\delta}, \qquad \gamma_R \sim \gamma_R^0 e^{+\lambda\delta}, \tag{2}$$

and thus the right tunnel rate, from the island to the drain, increases due to the smaller separation while the left tunnel rate decreases due to the larger separation. This is reversed if the motion is to the left (δ negative), or towards the source:

$$\gamma_L \sim \gamma_L^0 e^{+\lambda|\delta|}, \qquad \gamma_R \sim \gamma_R^0 e^{-\lambda|\delta|}. \tag{3}$$

Inserting these into (1), we easily get:

$$\Omega \equiv \frac{i^{\text{positive displacement}}}{i^{\text{negative displacement}}} = \frac{\gamma_L^0 e^{-\lambda|\delta|} + \gamma_R^0 e^{+\lambda|\delta|}}{\gamma_L^0 e^{+\lambda|\delta|} + \gamma_R^0 e^{-\lambda|\delta|}} = \frac{1 + F e^{+2\lambda|\delta|}}{e^{+2\lambda|\delta|} + F}, \tag{4}$$

where $F = \gamma_R^0/\gamma_L^0$. If $F = 1$ then $\Omega = 1$, and there is no difference between the currents in the two cases. When $F \gg e^{+2\lambda|\delta|}$, $\Omega \sim e^{+2\lambda|\delta|}$, while if $F \ll e^{-2\lambda|\delta|}$, $\Omega \sim e^{-2\lambda|\delta|}$, and in either of these asymmetric cases the two currents can be very different from each other if $\lambda|\delta|$ is appreciable.

In the sections below, we analyse the classical and quantum models of this system. Following the above simple rationale, we can find a realistic parameter range where the right-hand tunnel current shows a large (exponential), dependence on small spin-dependent island position displacements. This is confirmed below using low-resolution numerical simulations of both the 'semiclassical' and quantum systems, and through high-resolution quantum simulations. Besides demonstrating the two different current 'signals' corresponding to the spin force, we must also determine the noise present within the system to estimate the signal-to-noise ratio or so-called Fano factor. Following standard methods, we derive the current spectral noise density and from this the signal-to-noise properties of the coupled system. Using all this we finally deduce the measurement time required to distinguish the spin state from the current signals and can find device parameters where this acquisition time will be several tens of nanoseconds.

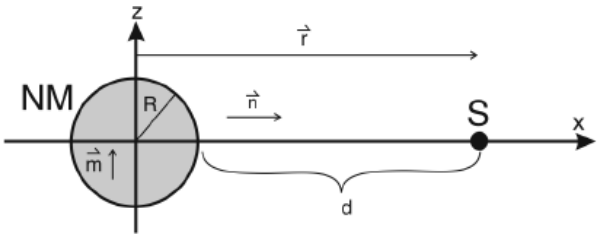

Figure 2. Schematic arrangement of the nanomagnet, as modelled by a small spherical ferromagnetic particle NM, of radius R, a distance d from the shuttle S. See section 2 for the computation of the spin-dependant force experienced by the shuttle due to the magnetic field gradient.

2. Magnetic field gradient

We now estimate the magnitude of the maximum magnetic field gradient we can achieve at the location of the shuttle. We follow a similar derivation in MRFM [50]. The Hamiltonian for the shuttle's endohedral spin, $\vec{S}$, interacting with a magnetic field which varies along the x-axis (see figure 2), $\vec{B}(x)$, is $H = -\vec{\mu} \cdot \vec{B} = -\mu_B g_e B(x) S_z$, while the resulting force on the shuttle is given by $F_{\text{spin}} = \mu_B g_e S_z \mathrm{d}B(x)/\mathrm{d}x$. If we consider placing a nanoscopic ferromagnetic spherical particle of radius R a distance d from the shuttle, one has

$$\vec{B}_{\text{Ferro}} = \frac{\mu_0}{4\pi} \frac{3\vec{n}(\vec{m} \cdot \vec{n}) - \vec{m}}{r^3}, \tag{5}$$

where $\mu_0 = 4\pi \times 10^{-7}\,\mathrm{H\,m^{-1}}$, $\vec{m}$ is the magnetic moment of the ferromagnetic particle, $\vec{r}$ is the vector connecting the particle to the shuttle and $r = |\vec{r}| = R + d$. For a sphere, the magnitude of the magnetic moment is $|\vec{m}| = 4/3\pi R^3 M$, where M is the magnetization of the ferromagnetic material. Following this, we have $\vec{B}_{\text{Ferro}} = -\mu_0 R^3 M / r^3 \hat{z}$. As the shuttle moves along the x-axis, the separations d and r, between the shuttle and the magnet change. Setting the distance between the shuttle and the magnet's centre to be $r \equiv R + d_0 + x = \bar{x} + x$, where x is the small oscillation of the shuttle, d_0 is the equilibrium separation, and $\bar{x} = R + d_0$, one can derive

$$F_{\text{spin}} = \frac{3\mu_B g_e \mu_0 M S_z}{\bar{x}} \left(\frac{R}{\bar{x}}\right)^3. \tag{6}$$

For an iron ferromagnet, $\mu_0 M = 2.2\,\text{tesla}$, and choosing $d_0 = 5\,\text{nm}$, $R = 5\,\text{nm}$, $\bar{x} = 10\,\text{nm}$, $S_z = \pm 3/2$ (for P@C_{60}), one obtains $F_{\text{spin}} \sim \pm 1 \times 10^{-15}\text{N}$.

Using this, we can re-examine the spin Hamiltonian and expand to first order in x about the equilibrium shuttle position, $H = -\mu_B g_e S_z B_z(r) = -\mu_B g_e S_z B_z(\bar{x} + x) \sim H_0 - F_{\text{spin}} x + \mathcal{O}(x^2)$, where H_0 is a constant which we drop. From (6), above we set

$$H_{\text{spin}} = -\tilde{\chi} S_z x, \tag{7}$$

where

$$\tilde{\chi} \equiv \frac{3\mu_e g_e \mu_0 M}{\bar{x}} \left(\frac{R}{\bar{x}}\right)^3. \tag{8}$$

The Hamiltonian for the Coulomb-energy of the charged island/shuttle can be written as

$$H_{\text{shuttle electronic}} = \hbar\omega_I c^\dagger c, \tag{9}$$

where c represents the operator which annihilates an electron on the shuttle, and $c^\dagger c$ is the number operator of injected electrons on the shuttle, which in the Coulomb blockade situation takes a value of either 0 or 1, while ω_I is the effective Coulomb self-energy of the excess electron on the shuttle (see section 5).

3. Electrostatic force

In most studies of electron shuttles [4]–[7],[13], one considers the shuttle to be driven primarily by the electrostatic force exerted on the shuttle through the interaction of the shuttle charge and an electric field present between the source and drain metallic contacts created by a potential difference $V = V_{\text{L}} - V_{\text{R}}$, across the inter-contact gap D. This gives an electric field of strength $E = V/D$.

In a standard treatment of electron shuttling [51], the shuttle acquires the electron at the average displacement of zero slightly towards the source and continues to move towards the source. It then undergoes electrostatic force to be propelled back towards the drain and loses the electron at a slightly displaced position towards the drain while continuing to move towards it. Again under electrostatic force, the shuttle moves back towards the source and repeats the process. In this case, no Harmonic restoring force is required to sustain the shuttle instability. However in our case, in the situation where our shuttle is operating in the Coulomb blockade regime, the shuttle can acquire a single excess negative charge near the source and thus be forced electrostatically to the drain, but once the shuttle dumps its electron at a displaced position near the drain there is no electrostatic force which can bring this shuttle back to the source contact to repeat the shuttle sequence. Thus in our case a Harmonic restoring force is required to sustain the shuttling action.

In more detail, $F_{\text{ES}} = qE = -eE$, where $E = -\mathrm{d}V/\mathrm{d}x \sim (V_{\text{R}} - V_{\text{L}})/D = -V/D$, if $V_{\text{L}} = -V_{\text{R}} = V/2$. Setting the potential due to this electrostatic force to be $\phi_{\text{ES}}(x)$, $F_{\text{ES}} = -\mathrm{d}\phi_{\text{ES}}/\mathrm{d}x$, and $\phi_{\text{ES}}(x) = -\int F_{\text{ES}}\,\mathrm{d}x = -qEx = |e|Ex = -|e|Vx/D$. Setting $\tilde{\eta} \equiv V|e|/D$, we have

$$H_{\text{ES}} = -\tilde{\eta}x. \tag{10}$$

4. Harmonic oscillator

The Hamiltonian of the harmonic oscillator is dealt with in the standard manner. Setting the annihilation operator for motional quanta to be, $\sqrt{2}a = x/x_0 + \mathrm{i}p/p_0$, where $x_0 = \sqrt{\hbar/(m\omega_0)}$ and $p_0 = \sqrt{m\omega_0\hbar}$ are the extents in x and p, of the ground state wavefunction of the harmonic oscillator, we have

$$H_{\text{HO}} = \frac{p^2}{2m} + \frac{k_0}{2}x^2 = \frac{p^2}{2m} + \frac{m\omega_0^2}{2}x^2 = \hbar\omega_0 a^\dagger a. \tag{11}$$

5. The model Hamiltonian

We are now in a position to write out the model Hamiltonian for the drain, source and motional, spin and electronic degrees of freedom of the shuttle. Recall that the Coulomb charge energy, U_c, the energy that is required to add an electron when there is already one electron occupying the shuttle (central island) is assumed to be large enough so that no more than one electron occupies the shuttle at any time. This is the Coulomb blockade regime. In this regime, the electronic state of the shuttle can be considered effectively in two states of $|0\rangle$ and $|1\rangle$, representing excess electron number state of the shuttle. So the effective Hamiltonian of the system, where the charging energy term is not explicitly expressed, can be written as

$$H = \hbar\omega_I c^\dagger c \tag{12}$$

$$- \chi\, S_z(a^\dagger + a)/\sqrt{2} \tag{13}$$

$$- \eta(a^\dagger + a)c^\dagger c/\sqrt{2} \tag{14}$$

$$+ \hbar\omega_0 a^\dagger a \tag{15}$$

$$+ \hbar \sum_{k_l} \omega^{\mathrm{L}}_{k_l} a^{\dagger\,\mathrm{L}}_{k_l} a^{\mathrm{L}}_{k_l} \tag{16}$$

$$+ \hbar \sum_{k_r} \omega^{\mathrm{R}}_{k_r} a^{\dagger\,\mathrm{R}}_{k_r} a^{\mathrm{R}}_{k_r} \tag{17}$$

$$+ \hbar \sum_{k_b} \omega_{k_b} b^\dagger_{k_b} b_{k_b} + \left(\sum_{k_i} a^\dagger b_{k_i} + \mathrm{h.c.} \right) \tag{18}$$

$$+ \sum_{k_{tl}} (T^{\mathrm{L}}_{k_{tl}} \hat{E}_{\mathrm{L}}(\hat{x}) a^{\mathrm{L}}_{k_{tl}} c^\dagger + \mathrm{h.c.}) \tag{19}$$

$$+ \sum_{k_{tr}} (T^{\mathrm{R}}_{k_{tr}} \hat{E}_{\mathrm{R}}(\hat{x}) a^{\mathrm{R}}_{k_{tr}} c^\dagger + \mathrm{h.c.}), \tag{20}$$

where $\chi \equiv \tilde{\chi} x_0$ and $\eta \equiv \tilde{\eta} x_0$. In the above Hamiltonian, $c^\dagger c$ and ω_I in (12) are respectively the number operator and the effective Coulomb self-energy of the excess electron on the shuttle. Equation (13) is the spin-dependent potential energy, (14) is the electrostatic potential energy, (15) is the harmonic oscillator self-energy, (16) and (17) are the self-energies of the Fermi baths in the source and drain contacts, (18) is the self-energy and coupling of a phonon bath to the motion of the shuttle, (19) is the tunnelling interaction between the source contact and the shuttle, while (20) is the tunnelling interaction between the shuttle and the drain contact.

We note the operators $\hat{E}_{\mathrm{L/R}}(\hat{x})$, in the tunnelling terms. The amplitude for tunnelling depends exponentially on the spatial separation between the source/drain and the shuttle. One can assume the forms

$$\hat{E}_{\mathrm{L}}(\hat{x}) = \gamma_{\mathrm{L}}^{1/2} \mathrm{e}^{-\tilde{\lambda}_{\mathrm{L}} x}, \qquad \hat{E}_{\mathrm{R}}(\hat{x}) = \gamma_{\mathrm{R}}^{1/2} \mathrm{e}^{+\tilde{\lambda}_{\mathrm{R}} x}, \tag{21}$$

where x is the displacement of the shuttle from its equilibrium position. In the following, we assume the source and drain are identical in shape and material and thus $\tilde{\lambda}_{\mathrm{L}} = \tilde{\lambda}_{\mathrm{R}} = \tilde{\lambda}$, where for Gold contacts, $\tilde{\lambda}^{-1} \sim 3$ Å. As above we set $\lambda \equiv \tilde{\lambda} x_0$ to get

$$\hat{E}_{\mathrm{L/R}} = \gamma_{\mathrm{L/R}}^{1/2} \exp(\mp\lambda(a^\dagger + a)/\sqrt{2}). \tag{22}$$

6. Displacement picture

As we mentioned above, the small static spin force exerted on the shuttle, in the absence of the electrostatic force, will cause a slight shift in the shuttle's equilibrium position within the Harmonic trapping potential. We now move to a frame of reference where we shift this displacement back to the origin. This can be done by considering the transformation

$$\rho \to \rho' = D(\alpha)\rho D^{\dagger}(\alpha), \tag{23}$$

where $D(\alpha) \equiv \exp(\alpha a^{\dagger} - \alpha^{*} a)$, is the standard displacement operator for operators satisfying $[a^{\dagger}, a] = 1$. By choosing $\alpha = -(\chi S_z)/(\sqrt{2}\hbar\omega_0)$, which corresponds to the physical displacement of the shuttle's equilibrium position due to the spin force F_{spin}, of

$$\tilde{\delta} = -\frac{F_{\text{spin}}}{m\omega_0^2}, \tag{24}$$

we can apply the displacement transformation (23), to the above full Hamiltonian to get

$$H' = \hbar\omega_I c^{\dagger} c \pm \delta\eta c^{\dagger} c \tag{25}$$

$$- \eta(a^{\dagger} + a)c^{\dagger} c/\sqrt{2} \tag{26}$$

$$+ \hbar\omega_0 a^{\dagger} a \tag{27}$$

$$+ \hbar \sum_{k_l} \omega_{k_l}^{\mathrm{L}} a_{k_l}^{\dagger\,\mathrm{L}} a_{k_l}^{\mathrm{L}} \tag{28}$$

$$+ \hbar \sum_{k_r} \omega_{k_r}^{\mathrm{R}} a_{k_r}^{\dagger\,\mathrm{R}} a_{k_r}^{\mathrm{R}} \tag{29}$$

$$+ \hbar \sum_{k_b} \omega_{k_b} b_{k_b}^{\dagger} b_{k_b} + \left(\sum_{k_i} a^{\dagger} b_{k_i} + \text{h.c.} \right) \tag{30}$$

$$+ \sum_{k_{tl}} (T_{k_{tl}}^{\mathrm{L}} \hat{E}_{\mathrm{L}}(\hat{x}') a_{k_{tl}}^{\mathrm{L}} c^{\dagger} + \text{h.c.}) \tag{31}$$

$$+ \sum_{k_{tr}} (T_{k_{tr}}^{\mathrm{R}} \hat{E}_{\mathrm{R}}(\hat{x}') a_{k_{tr}}^{\mathrm{R}} c^{\dagger} + \text{h.c.}), \tag{32}$$

where the spin-dependent term of $\delta \equiv \tilde{\delta}/x_0$ in (25) acquires explicitly opposite signs depending on the spin polarizations, and

$$\hat{E}_{\mathrm{L}}(\hat{x}') = \gamma_{\mathrm{L}}^{1/2} \exp(-\lambda[(a^{\dagger} + a)/\sqrt{2} \mp \delta]) \equiv \gamma_{\mathrm{L}}^{1/2} E_{\mathrm{L}}, \tag{33}$$

$$\hat{E}_{\mathrm{R}}(\hat{x}') = \gamma_{\mathrm{R}}^{1/2} \exp(+\lambda[(a^{\dagger} + a)/\sqrt{2} \mp \delta]) \equiv \gamma_{\mathrm{R}}^{1/2} E_{\mathrm{R}}. \tag{34}$$

7. Master equation

Assuming that the timescales for the couplings to the source, drain and phonon baths are faster than those associated with the harmonic oscillator and electrostatic potential, one can derive the following master equation [51]:

$$\frac{\mathrm{d}\rho}{\mathrm{d}t} = -\mathrm{i}\omega_0[a^\dagger a, \rho] + \mathrm{i}\frac{\eta}{\hbar}[(a^\dagger + a)c^\dagger c/\sqrt{2}, \rho] \tag{35}$$

$$+ \gamma_\mathrm{L}\{f_\mathrm{L}(\omega_I \mp \delta\eta)\mathcal{D}[c^\dagger E_\mathrm{L}]\rho + (1 - f_\mathrm{L}(\omega_I \mp \delta\eta))\mathcal{D}[cE_\mathrm{L}]\rho\} \tag{36}$$

$$+ \gamma_\mathrm{R}\{f_\mathrm{R}(\omega_I \mp \delta\eta)\mathcal{D}[c^\dagger E_\mathrm{R}]\rho + (1 - f_\mathrm{R}(\omega_I \mp \delta\eta))\mathcal{D}[cE_\mathrm{R}]\rho\} \tag{37}$$

$$+ \kappa(\bar{N} + 1)\mathcal{D}[a]\rho + \kappa\bar{N}\mathcal{D}[a^\dagger]\rho, \tag{38}$$

where the super-operator $\mathcal{D}$ is defined to be $\mathcal{D}[A]B \equiv ABA^\dagger - \frac{1}{2}(A^\dagger AB + BA^\dagger A)$. The mean excitation of the thermal bath is $\bar{N} = 1/\exp(\hbar\omega_0/k_\mathrm{B}T - 1)$ and $f(x) = (\exp(x/(k_\mathrm{B}T)) + 1)^{-1}$, is the Fermi factor where

$$f_\mathrm{L}(\omega_I \mp \delta\eta) = f(\omega_I \mp \delta\eta - \mu_\mathrm{L}) = f(\omega_I \mp \delta\eta - V/2), \tag{39}$$

$$f_\mathrm{R}(\omega_I \mp \delta\eta) = f(\omega_I \mp \delta\eta - \mu_\mathrm{R}) = f(\omega_I \mp \delta\eta + V/2), \tag{40}$$

with a dependence on the bias voltage (through the chemical potential). Here we have ignored co-tunnelling and higher order tunnelling events, so the master equation applies under weak tunnelling conditions. Notice the dependency of the Fermi factor on the spin force. If the displacement factor δ is large enough, the Fermi energies corresponding to the two spin directions will become significantly different and large enough to be observable at low temperatures. If one supposes that the bias voltage can be tuned to be between these two energies such that only one Fermi factor (corresponding to spin up say), is near unity while the other is nearly vanishing, it should be possible to differentiate the two spins based on the detection or absence of current. However, with such low bias, we believe the noise in the system will be overwhelming and we thus proceed by assuming that the system is in large bias such that this effect is negligible.

Now at milli-Kelvin temperatures, $k_\mathrm{B}T \sim 0.2\,\mu$eV, while $\omega_I \sim 5$ meV. So if $V > 10$ meV then $f_\mathrm{L} \to 1$, while $f_\mathrm{R} \to 0$, giving the simpler form for the master equation:

$$\frac{\mathrm{d}\rho}{\mathrm{d}t} = -\mathrm{i}\omega_0[a^\dagger a, \rho] + \mathrm{i}\frac{\eta}{\hbar}[(a^\dagger + a)c^\dagger c/\sqrt{2}, \rho] + \gamma_\mathrm{L}\mathcal{D}[c^\dagger E_\mathrm{L}]\rho + \gamma_\mathrm{R}\mathcal{D}[cE_\mathrm{R}]\rho + \kappa(\bar{N} + 1) \times\mathcal{D}[a]\rho + \kappa\bar{N}\mathcal{D}[a^\dagger]\rho. \tag{41}$$

This master equation is different from the semiclassical equations used, for example, in [4]–[7] where the mechanical motion is treated classically and dynamical variables are treated as parameters in the framework of the orthodox Coulomb blockade theory. This master equation is, however, similar to the generalized master equation of quantum shuttles used in [27, 34], where the mechanical motion is quantized and dynamical variables are treated as operators. In our case, the tunnelling probabilities depend exponentially not only on the shuttle–electrode separations but also on the spin polarizations of the excess electron on the shuttle. In addition,

to show and derive the conditions that the spin state can be distinguished in large magnetic field gradient from the the resulting current signals, we will also analyse the dynamics using the master equation (41).

8. Expectation values

From the master equation (41), we can derive the following differential equations:

$$\frac{\mathrm{d}\langle c^\dagger c\rangle}{\mathrm{d}t} = \gamma_\mathrm{L}\langle \hat{E}_\mathrm{L}^\dagger E_\mathrm{L}(1-c^\dagger c)\rangle - \gamma_\mathrm{R}\langle E_\mathrm{R}^\dagger \hat{E}_\mathrm{R} c^\dagger c\rangle, \tag{42}$$

$$\frac{\mathrm{d}\langle x/x_0\rangle}{\mathrm{d}t} = \omega_0\left\langle \frac{p}{p_0}\right\rangle - \frac{\kappa}{2}\left\langle \frac{x}{x_0}\right\rangle, \tag{43}$$

$$\frac{\mathrm{d}\langle p/p_0\rangle}{\mathrm{d}t} = -\omega_0\left\langle \frac{x}{x_0}\right\rangle + \bar{F}_\mathrm{ES}\langle c^\dagger c\rangle - \frac{\kappa}{2}\left\langle \frac{p}{p_0}\right\rangle, \tag{44}$$

where

$$\bar{F}_\mathrm{ES} \equiv \frac{V|e|}{Dp_0} = \frac{|F_\mathrm{ES}|}{p_0}. \tag{45}$$

These equations can be further tidied by going to natural time units associated with the harmonic oscillator, i.e. $\tau = \omega_0 t$, and by defining

$$\bar{\gamma}_\mathrm{L/R} = \frac{\gamma_\mathrm{L/R}}{\omega_0}, \qquad \bar{\kappa} = \frac{\kappa}{2\omega_0}, \qquad \bar{\chi}_\mathrm{ES} = \frac{\bar{F}_\mathrm{ES}}{\omega_0}, \tag{46}$$

we get

$$\frac{\mathrm{d}\langle c^\dagger c\rangle}{\mathrm{d}\tau} = \bar{\gamma}_\mathrm{L}\mathrm{e}^{\pm 2\lambda\delta}\langle \mathrm{e}^{-2\lambda x/x_0}(1-c^\dagger c)\rangle - \bar{\gamma}_\mathrm{R}\mathrm{e}^{\mp 2\lambda\delta}\langle \mathrm{e}^{+2\lambda x/x_0} c^\dagger c\rangle, \tag{47}$$

$$\frac{\mathrm{d}\langle x/x_0\rangle}{\mathrm{d}\tau} = \left\langle \frac{p}{p_0}\right\rangle - \bar{\kappa}\left\langle \frac{x}{x_0}\right\rangle, \tag{48}$$

$$\frac{\mathrm{d}\langle p/p_0\rangle}{\mathrm{d}\tau} = -\left\langle \frac{x}{x_0}\right\rangle + \bar{\chi}_\mathrm{ES}\langle c^\dagger c\rangle - \bar{\kappa}\left\langle \frac{p}{p_0}\right\rangle. \tag{49}$$

The above equations cannot be solved as they are not closed. We first take the semiclassical approach by factorizing the moments of oscillator and electronic degrees of freedom. This ignores any entanglement between these systems. We then factorizing the exponential $\langle \mathrm{e}^{\pm 2\lambda x/x_0}\rangle \approx \mathrm{e}^{\pm 2\lambda\langle x/x_0\rangle}$. This assumes the oscillator is very well localized in position. These factorizations may become a good approximation when the mechanical damping is large and the electron tunnelling rates are large compared to the natural frequency of the oscillator [51]. When these

are done, we finally obtain:

$$\begin{aligned}
\frac{\mathrm{d}\langle c^\dagger c\rangle}{\mathrm{d}\tau} &= \bar{\gamma}_{\mathrm{L}} \mathrm{e}^{\pm 2\lambda\delta} \mathrm{e}^{-2\lambda\langle x/x_0\rangle}(1-\langle c^\dagger c\rangle) - \bar{\gamma}_{\mathrm{R}} \mathrm{e}^{\mp 2\lambda\delta} \mathrm{e}^{+2\lambda\langle x/x_0\rangle}\langle c^\dagger c\rangle,\\
\frac{\mathrm{d}\langle x/x_0\rangle}{\mathrm{d}\tau} &= \left\langle \frac{p}{p_0}\right\rangle - \bar{\kappa}\left\langle \frac{x}{x_0}\right\rangle,\\
\frac{\mathrm{d}\langle p/p_0\rangle}{\mathrm{d}\tau} &= -\left\langle \frac{x}{x_0}\right\rangle + \bar{\chi}_{\mathrm{ES}}\langle c^\dagger c\rangle - \bar{\kappa}\left\langle \frac{p}{p_0}\right\rangle,
\end{aligned} \tag{50}$$

while the complete master equation in these rescaled parameters takes the form,

$$\begin{aligned}
\frac{\mathrm{d}\rho}{\mathrm{d}\tau} = &-\mathrm{i}[a^\dagger a,\rho] + \mathrm{i}\chi_{\bar{\mathrm{E}}S}[(a^\dagger + a)c^\dagger c/\sqrt{2},\rho]/\hbar + \mathcal{D}[c^\dagger E_{\mathrm{L}}]\rho + \mathcal{D}[cE_{\mathrm{R}}]\rho + \kappa(\bar{N}+1)\\
&\times\mathcal{D}[a]\rho + \kappa\bar{N}\mathcal{D}[a^\dagger]\rho,
\end{aligned} \tag{51}$$

where

$$E_{R/\mathrm{L}} \equiv \sqrt{\bar{\gamma}_{R/\mathrm{L}}}(c/c^\dagger)\exp\left[\mp\lambda\delta \pm \lambda(a+a^\dagger)/\sqrt{2}\right]. \tag{52}$$

In what follows, we take the phonon bath to be at zero temperature $\bar{N}=0$, and that the typical phonon bath excitation will have energies much smaller than that of the oscillator, i.e. below 1 GHz.

We will, in particular, be interested in the 'semiclassical' and fully quantum steady-state behaviour of the right tunnel current, or the expected value of the operator:

$$\bar{i}_{\mathrm{R}} \equiv \frac{\omega_0}{e} i_{\mathrm{R}} \equiv \bar{\gamma}_{\mathrm{R}} \mathrm{e}^{\mp 2\lambda\delta} \mathrm{e}^{+2\lambda x/x_0} c^\dagger c = \bar{\gamma}_{\mathrm{R}} \mathrm{e}^{\mp 2\lambda\delta} \mathrm{e}^{+2\lambda\bar{x}} c^\dagger c, \tag{53}$$

where $\bar{x} \equiv x/x_0$, $\bar{p} \equiv p/p_0$, and $\bar{i}_{\mathrm{R}}$, is the rescaled average current flowing from the moving island to the drain. We wish to determine whether $\langle \bar{i}_{\mathrm{R}}(t\to\infty)\rangle = \langle \bar{i}_{\mathrm{R}}^{\infty}\rangle$, is *significantly* different in the two cases when the endohedral spin is up or down. However it is not enough that the two currents (endohedral spin up/down), are different but we must also then determine the steady-state (or DC or zero-frequency), quantum noise associated with these two steady-state currents. This DC noise will allow us to determine how *distinguishable* the two current signals are. This then will determine the minimum length of signal acquisition time one can average over to achieve a signal-to-noise ratio which will allow the endohedral spin states to be distinguished to a high level of confidence. In the following subsection (9.2), we discuss the initial 'semi-classical' and quantum mechanical steady-state for the coupled electronic–vibronic shuttle system, paying particular regard to the change in right tunnel current with endohedral spiTn-state. This is done in a parameter range of the system where we are certain that our numerics are very precise and faithfully simulate the system. We find a parameter regime where $\langle \bar{i}_{\mathrm{R}}^{\uparrow}\rangle/\langle \bar{i}_{\mathrm{R}}^{\downarrow}\rangle$ can be substantial, indicating that the endohedral spin-state measurement could be possible. In the subsection (9.3), we expand the size of the numerical simulation to cover a much larger range of parameters (see parameter set (B) in table 1), which models a much larger electrostatic drive force $\bar{\chi}_{\mathrm{ES}}$. This is done using the method of quantum trajectories or stochastic Schrödinger equation [52]–[67]. This type of simulation is very costly and only a small number of such simulations were performed. We found that when the electrostatic driving force is increased, the ratio $\langle \bar{i}_{\mathrm{R}}^{\uparrow}\rangle/\langle \bar{i}_{\mathrm{R}}^{\downarrow}\rangle$ remains significant. Further, the highly accurate quantum trajectory simulations correspond very well with the lower-resolution steady-state results indicating that our steady-state numerics could

Table 1. Parameter values for the model (A) typical physical parameters, (B) initial model parameters studied in 'semiclassical' and quantum steady state, numerical analyses, (C) parameters used in 'semiclassical', low-resolution quantum steady-state, and high-resolution quantum dynamical (quantum trajectory), numerical analyses.

	λ	δ	$\bar{\chi}_{ES}$	$\bar{\kappa}$	$\bar{\gamma}_L$	$\bar{\gamma}_R$
A	0.4	0.18	28	2	0.1	0.9
B	0.4	0.4	2	2	0.1	0.9
C	0.4	0.4	10	2	0.1	0.8

be trusted to quite large values of the electrostatic force. In the subsection (9.4), we derive the analytical expressions for the noise spectra and numerically derive the DC-noise component over a limited (but precisely modelled) range of parameters. We reproduced the expected values for the DC noise of a standard, spatially fixed quantum dot, in the case when $\lambda = 0$, i.e. no coupling between the electronic and vibration degrees of freedom. We further found a slight decrease in this noise with the amount of electrostatic driving and degree of the exponential coupling. Finally, in the subsection (9.5), we gather together all this information to estimate the measurement time required to distinguish between the current signals due to endohedral spin up(down).

9. Numerical analysis

9.1. Physical parameters

We now determine the typical values of the dimensionless parameters appearing in the system's dynamics. We will take, $m_{C_{60}} = 1.2 \times 10^{-24}\,\mathrm{kg}$, $\omega_0 = 2\pi \times 1\,\mathrm{GHz}$, the potential difference between the contacts to be $V = 10\,\mathrm{meV}$, and the spatial separation between the contacts $D = 10\,\mathrm{nm}$. From this we have $x_0 \sim 1.2\,\text{Å}$, $\delta \sim 0.18$, giving the physical displacement $\bar{\delta} \sim 0.2\,\text{Å}$. The dimensionless displacement of the harmonically bound shuttle due to the electrostatic force alone in units of x_0 is $\delta_{ES} \sim |F_{ES}|/(m\omega_0^2 x_0) \sim 28$, while $\lambda \sim 0.4$. From symmetry conditions, one might suspect that we cannot gain any advantage from the exponential dependence of the tunnelling amplitudes on the shuttle-contact separation if the shuttle's equilibrium position is exactly midway between the contacts (effectively when $\bar{\gamma}_L = \bar{\gamma}_R$). Thus we choose $\bar{\gamma}_L \sim 0.1$, while $\bar{\gamma}_R \sim 0.9$. We choose $\bar{\kappa} \sim 2$, thus setting the system close to critical damping. We also set $\bar{N} = 0$, or assume a zero temperature vibronic bath, throughout. The example rescaled parameter values that we study below are summarized in table 1.

9.2. Semi-classical and quantum steady-state

From equation (50), one can obtain the steady-state solution for the expectation values of $\bar{n} = \langle c^\dagger c \rangle$, $\langle \bar{x} \rangle$, and $\langle \bar{p} \rangle$, to be

$$\langle \bar{n} \rangle_\infty = \frac{1}{\gamma_R/\gamma_L e^{4\lambda \bar{x}_\infty \pm 4\lambda\delta}}, \tag{54}$$

$$\langle \bar{x} \rangle_\infty = \frac{\bar{\chi}_{\rm ES}}{[1 + (\kappa/2)^2]} \bar{n}_\infty, \tag{55}$$

$$\langle \bar{p} \rangle_\infty = \kappa \bar{n}_\infty. \tag{56}$$

Thus the fixed point must satisfy:

$$\bar{x}_\infty = \frac{\bar{\chi}_{\rm ES}}{1 + (\kappa/2)^2} \left(\frac{1}{\gamma_{\rm R}/\gamma_{\rm L} {\rm e}^{4\lambda \bar{x}_\infty \pm 4\lambda\delta}} \right). \tag{57}$$

Following the derivation outlined in [51], the stability of the fixed point can be found by looking at the eigenvalues derived from a linearized dynamics. From [51], the system possesses one real eigenvalue and two complex conjugate eigenvalues which indicate the existence of a limit cycle. This limit cycle appears at a bifurcation of the fixed point which happens when the eigenvalues are purely imaginary. This condition appear at a critical value of $\chi_{\rm ES}$:

$$\chi_{\rm ES} \equiv \chi_{\rm h} = \frac{(A_*^2 + A_* \kappa + (\kappa/2)^2 + 1) A_* \kappa}{4\lambda \gamma_{\rm L} \gamma_{\rm R}}, \tag{58}$$

where $A_* = \gamma_{\rm L} {\rm e}^{-2\lambda \bar{x} \mp 2\lambda\delta} + \gamma_{\rm R} {\rm e}^{2\lambda \bar{x} \pm 2\lambda\delta}$.

Interestingly, the fixed point for the two spins are different and will result in a slightly different critical $\chi_{\rm h}$ values. However we choose to operate away from this regime in order to again avoid any possibility of noise upsetting the distinguishability of the resulting signals.

A more straight forward method is to keep the system such that it falls within the fixed point regime and proceeds in calculating the difference in the steady-state current. This is possible by a careful choice of values such that the coupling $\chi_{\rm ES}$ are always below this critical values for both of the spins. This puts the system well in the supercritical regime. We can thus proceed by looking at the steady state at the fixed point and thus eliminating the possible error related to the existence of a stable limit cycle at the outer position of the doped fullerene's oscillations.

From (54)–(56), we see that when $\lambda = 0$, there is obviously no dependence of the current on the endohedral spin-state when $\bar{\gamma}_{\rm R} = \bar{\gamma}_{\rm L}$. This is not the case when the coupling is non-vanishing i.e. $\lambda > 0$. This reflects the inherent asymmetry of the current transport from the source to the drain which is now mediated by an island which has, essentially, steady-state tunnelling probabilities to either contact which are now effected by the endohedral spin dependent equilibrium position of the island. Taking, the steady-state semiclassical right tunnel current to be $\langle \bar{i}_{\rm R} \rangle_\infty^{\rm SC} = \bar{\gamma}_{\rm R} \exp(\pm 2\delta\lambda) \langle \bar{n} \rangle_\infty$, we have

$$\frac{\langle \bar{i}_{\rm R}^{\uparrow} \rangle_\infty^{\rm SC}}{\langle \bar{i}_{\rm R}^{\downarrow} \rangle_\infty^{\rm SC}} = \frac{\bar{\gamma}_{\rm L} {\rm e}^{+2\lambda\delta} + \bar{\gamma}_{\rm R} {\rm e}^{-2\lambda\delta}}{\bar{\gamma}_{\rm L} {\rm e}^{-2\lambda\delta} + \bar{\gamma}_{\rm R} {\rm e}^{+2\lambda\delta}} \sim {\rm e}^{-4\lambda\delta}, \tag{59}$$

in the limit of large $\bar{\gamma}_{\rm R}/\bar{\gamma}_{\rm L}$ ($\bar{\Gamma}_{\rm R}/\bar{\Gamma}_{\rm L} \gg {\rm e}^{+4\lambda\delta}$), and large $\lambda\delta$. Thus we might expect an exponential dependance of the resulting current ratio on the endohedral spin-state.

We can obtain the steady-state solution to (51), by converting the resulting master equation into a $4N^2 \times 4N^2$, (where N is the size of the truncation of the Fock-state representation of the vibronic Hilbert space), complex matrix and searching for the eigenstate (ρ_∞), with vanishing eigenvalue. We use the inverse power method to find the eigenvector with smallest eigenvalue [68]. In the following we mostly choose $N = 36$, giving matrices of size $4096 \times 4096 \sim 256$ MB

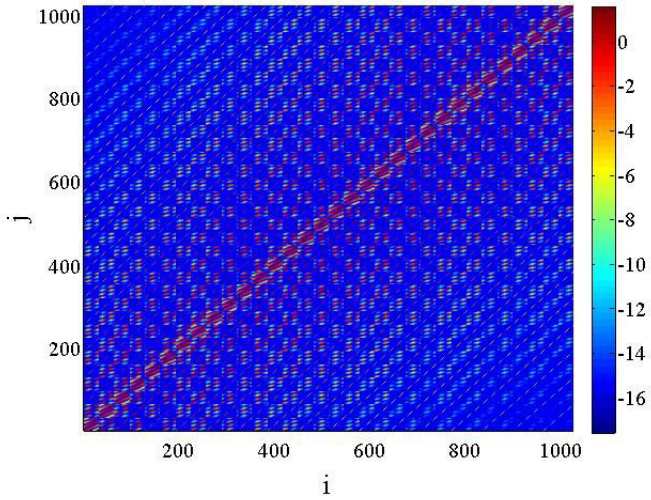

Figure 3. Plot illustrating the non-sparse characteristics of the Liouvillian superoperator $\mathcal{L}$, corresponding to equation (41), $\mathrm{d}\rho/\mathrm{d}t = \mathcal{L}(\rho)$. We plot $\log_{10}$ of $|\mathcal{L}_{ij}|$, for $\rho \in \mathcal{H}_e \otimes \mathcal{H}_{vib}$, when expanded into a $4N^2 \times 4N^2$ matrix with a truncation of the vibrational Hilbert space to include only the lowest $N = 16$ Fock states. The steady-state solution is the eigenvector with vanishing eigenvalue of this matrix. We note the non-trivial band structure of this superoperator.

in memory. As the memory resources increase with N^4, we cannot realistically go beyond $N \sim 60$. However, if the resulting large matrix is sparse then routines which only use matrix vector products can be used to determine the steady-state solution [69]. In figure 3, we see that although the matrix has many small elements, it is unclear that it is highly sparse. As the current (53), is exponential in $\bar{x}$, the expectation value $\langle \bar{i}_R \rangle$, could depend on very small matrix elements. To ensure convergence we will work with the full matrix in what follows and choose to truncate the bosonic vibrational Hilbert space at $N = 16$ or 32.

In figure 4, we plot the 'semiclassical' evolution of (50), and quantum steady-state expectation values when $\bar{\chi}_{ES} = 3$, $\bar{\kappa} = 1$, $\bar{\gamma}_L = 0.1$, $\bar{\gamma}_R = 0.9$ and $\lambda = \delta = 0.4$. We see that the different endohedral spin states lead to very different phase space dynamics, differing island populations $\langle \bar{n} \rangle$, and currents $\langle \bar{i}_R \rangle_\infty$. One further notices a remarked difference between the magnitudes of the quantum and semiclassical expectation values for the currents in figure (4(C)). This difference grows with the size of $\bar{\chi}_{ES}$, and is primarily due to the extended nature of the quantum state in the vibronic phase space. With the availability of the full quantum steady-state solution we are also able to visualize the quantum state via quasi-distribution functions and in figure 5, we see that the quantum state is localized near the phase space origin. Moreover, from the compactness of the resulting Wigner or Husimi representations we can be relatively certain that the quantum steady-state solution is well represented with a Fock state truncation level set at $N = 32$. As $\bar{\chi}_{ES}$ is increased towards the more physically realistic regime of $\bar{\chi}_{ES} \sim 20$, one is justifiably concerned whether a truncation level of $N \sim 32$, would remain sufficient to accurately represent the resulting quantum steady-state solution. We will see below however, that $N \sim 32$, remains fairly accurate when $\bar{\chi}_{ES} = 10$. In the section below we are primarily interested in knowing with relative certainty that our quantum simulations are highly accurate. In figure 6,

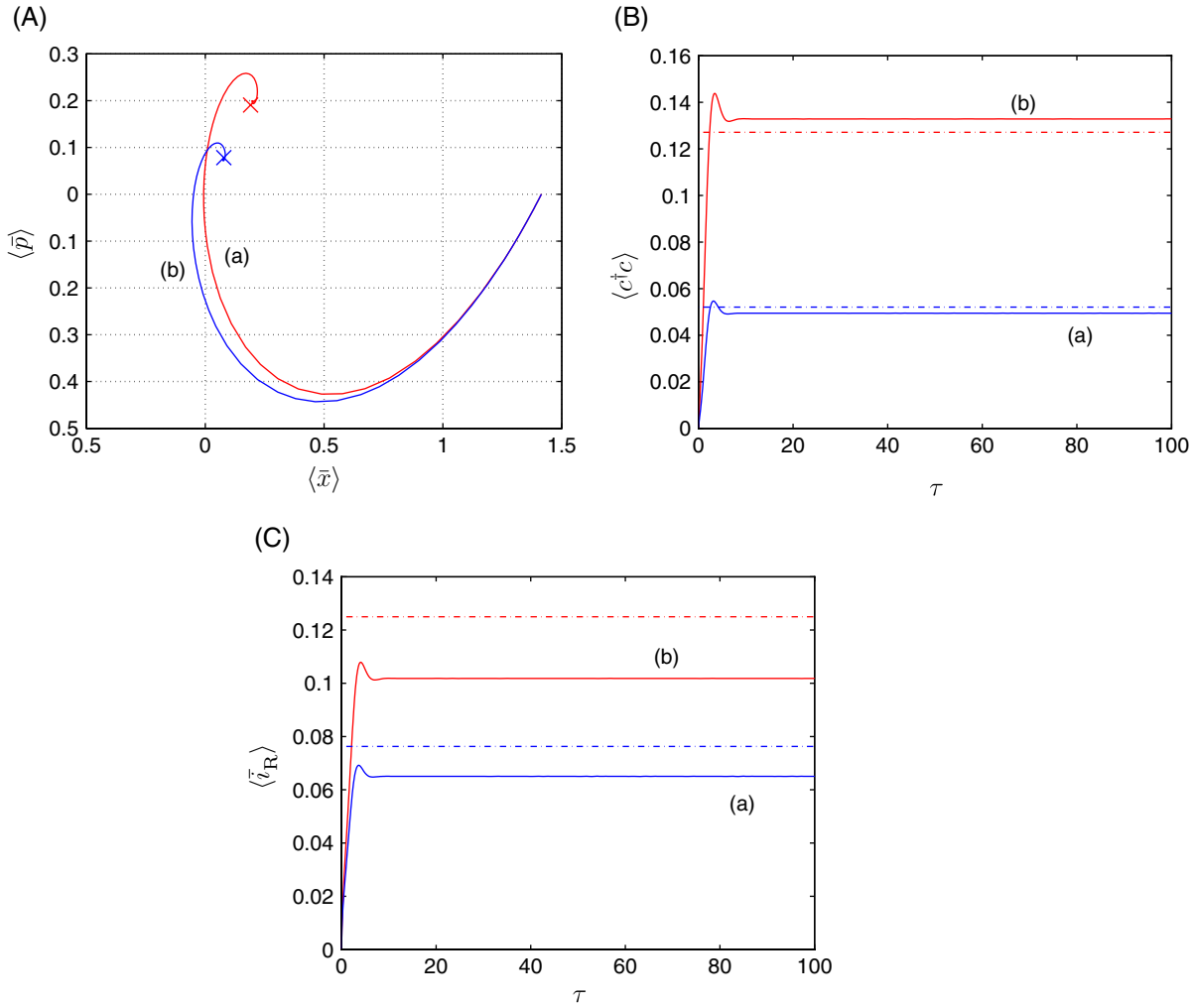

Figure 4. Semiclassical and steady-state quantum expectation values for the case $\bar{\chi}_{ES} = 3,\ \bar{\kappa} = 1,\ \bar{\gamma}_L = 0.1,\ \bar{\gamma}_R = 0.9$ and $\lambda = \delta = 0.4$. (A) semiclassical phase space evolution (in displaced picture), (a)/(b) correspond to spin up/down or $\pm\delta$; (B) graphs of $\langle c^\dagger c \rangle$, for the two endohedral spin states (a) and (b), and where solid curves are the semiclassical solutions and the dashed are the quantum steady-state expectation values with $N = 32$; (C) graphs of $\langle \bar{i}_R \rangle$, for the two endohedral spin states (a) and (b), and where solid curves are the semiclassical solutions and the dashed are the quantum steady-state expectation values with $N = 32$.

we superimpose the semiclassical phase space evolution on to the Wiger function of the quantum steady-state solution for the two cases of endohedral spin up and down. We note that due to a slight asymmetry in the Wigner function the quantum expectation value for the steady-state equilibrium solution is not located at the peak of the Wigner function.

We can see from this analysis that there is a significant difference between $\langle \bar{i}_R^{\uparrow} \rangle$, and $\langle \bar{i}_R^{\downarrow} \rangle$. To characterize this difference more systematically, we numerically evaluate the ratio $\langle \bar{i}_R^{\uparrow} \rangle / \langle \bar{i}_R^{\downarrow} \rangle$, as a function of $\bar{\gamma}_L$ and $\bar{\gamma}_R$. We choose $\bar{\chi}_{ES} = 3,\ \bar{\kappa} = 2,\ \lambda = \delta = 0.4$, and range through values

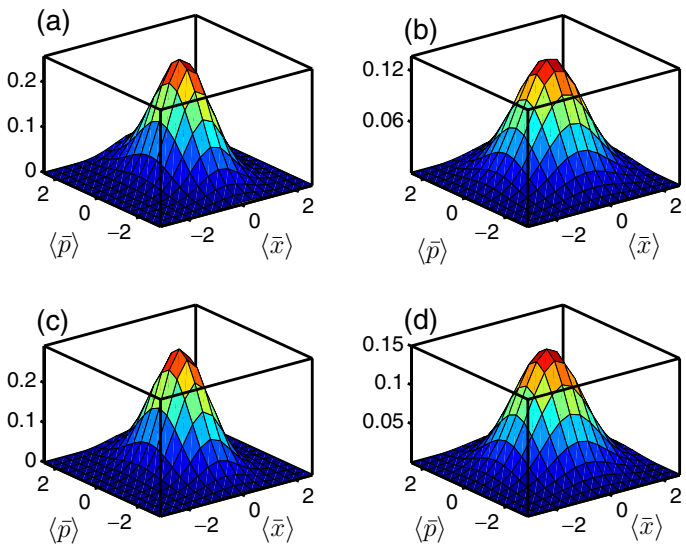

Figure 5. Plot of the quasi-distribution functions for the quantum steady-state of the motional state of the shuttle. Graphs (a) and (c) are Wigner functions of the reduced vibronic steady-state, $\rho_\infty^{\text{vib}} = \text{Tr}_{\text{dot}}[\rho_\infty]$, for the cases of endohedral spin up and down (same parameter values as in figure 4); (b) and (d) are Husimi function for same. The compactness of these distributions indicates the good convergence of our numerics for the parameter values chosen.

of $\bar{\gamma}_\text{L}$ and $\bar{\gamma}_\text{R}$, computing the resulting quantum steady-state current ratios for the two cases of endohedral spin up and spin down. The results are shown in figure 7, and in the limit of large $\bar{\gamma}_\text{R}/\bar{\gamma}_\text{L}$ ($\bar{\Gamma}_\text{R}/\bar{\Gamma}_\text{L} \gg \text{e}^{+4\lambda\delta}$), the current ratio appears to asymptote, as it should to $\exp(4\lambda\delta) \sim 1.9$. By repeating these simulations at the reduced truncation $N = 16$, and finding that the resulting current ratios are within 10^{-9} of those computed at $N = 32$, indicates that our quantum steady-state simulations are extremely precise.

9.3. Quantum trajectories

As mentioned above, going much beyond a Fock state truncation of $N \sim 60$, with the full matrix representation of the Liouvillian is not possible without exotic computational resources. For numerical purposes, it is often much easier to solve an equation for a pure state vector rather than for a density matrix. It is therefore useful to unravel the quantum master equation of the reduced density matrix into a stochastic Schrödinger equation which preserves pure states. For an N-dimensional Hilbert space, the stochastic Schrödinger equation evolves an N-dimensional vector and thus offers numerical advantages over a master equation which evolves an $N \times N$ density matrix. This method of simulating the dynamics of the full quantum master equation (51) using pure state evolutions, is called *quantum trajectories* or *stochastic Schrödinger equation* [52]–[67]. In this method, one represents the quantum master equation (51), as an average of a stochastic Schrödinger equation over some stochastic noise. The temporal evolution of an initial state determined by a stochastic Schrödinger equation through a particular realization of stochastic noise is known as a quantum trajectory. One can determine the time evolution of quantum expectation values of an observable by taking the expectation values of that observable

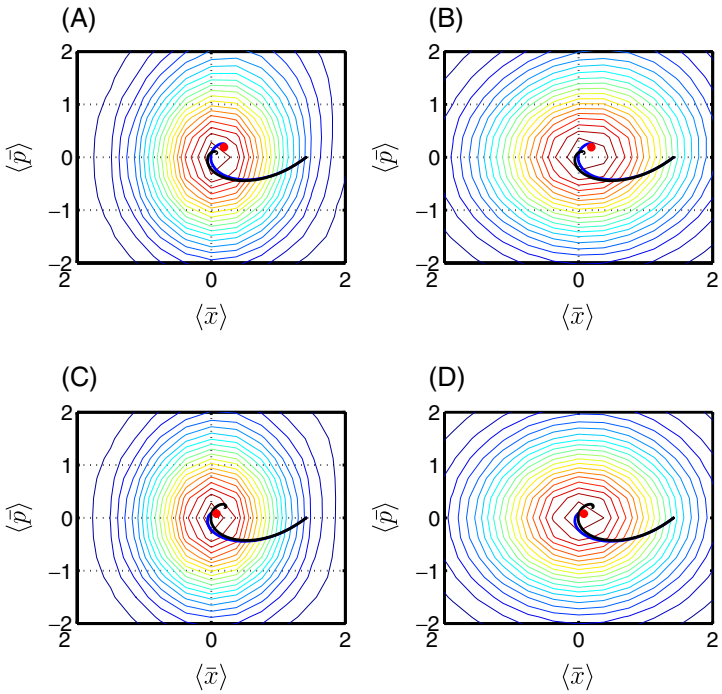

Figure 6. Semiclassical dynamics overlayed with the quantum steady-state. Graphs (A) and (C) are the semiclassical (blue/black curves), quantum steady-state phase point $(\langle\bar{x}\rangle_\infty, \langle\bar{p}\rangle_\infty)$, as a red symbol, and the contours of the quantum steady-state Wigner function, for the case of endohedral spin up and down. The blue curve is the appropriate semiclassical phase space trajectory for the spin up(down), while the black curve is the other case shown for comparison. Graphs (B) and (D) are same except the Husimi function is used.

within a single quantum trajectory and then averaging the expectation values found over numerous stochastic realizations of the quantum trajectories. Again, since the method primarily involves the Schrödinger evolution of pure quantum states, the quantum evolution of an individual quantum trajectory can be simulated with much higher Fock state truncations N, than in the above steady-state density matrix method. The down side is that to obtain precise expectation values, one must average over a large number of realizations of the quantum trajectories.

The method of quantum trajectories can also be used to describe the dynamics of the quantum system conditioned on a measurement record [51], [61]–[66]. The evolution of the stochastic Schrödinger equation corresponding to (51), when $\bar{N} = 0$, is conditioned on the appearance of random quantum jumps. The information gained by the environment, in a sense, yields information which conditions the quantum state following the quantum jump. In (51), there are three types of quantum jumps: (i) $|\psi\rangle \to c^\dagger E_{\rm L}|\psi\rangle$ (unnormalized), which corresponds to an electron tunnelling on to the island from the Fermi bath of the left electrode with some associated monitoring (via $E_{\rm L}$), of the island's position state by the vibrational bath, (ii) $|\psi\rangle \to cE_{\rm R}|\psi\rangle$, corresponding to an electron moving off the island into the Fermi bath of the right electrode with some associated monitoring (via $E_{\rm R}$), of the island's position state by the vibrational bath, and (iii) $|\psi\rangle \to a|\psi\rangle$, where a motional quanta escapes from the island's position state into the

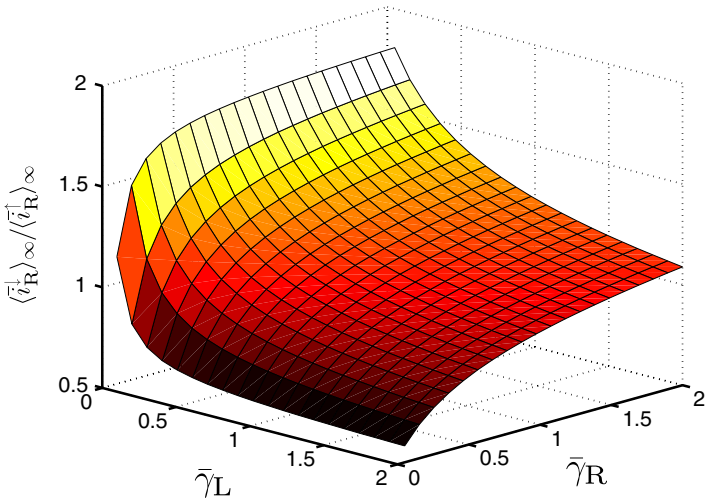

Figure 7. Graph of $\langle \bar{i}_R^{\downarrow} \rangle_\infty / \langle \bar{i}_R^{\uparrow} \rangle_\infty$, computed via the quantum steady-state for a range of values of the left and right tunnel amplitudes, $\bar{\gamma}_L$ and $\bar{\gamma}_R$, for $\bar{\chi}_{ES} = 3$, $\bar{\kappa} = 2$, $\lambda = \delta = 0.4$ (see section 9.2). For large $\bar{\gamma}_R / \bar{\gamma}_L$, the ratio tends to $\exp(+4\lambda\delta)$, as predicted by equation (59).

vibrational bath. In figure 8, we show an example of a single quantum trajectory of the coupled electronic–vibronic shuttle system corresponding to (51). We choose no motional damping and set most of the parameters to vanish, so we can illustrate the effects of the quantum jumps clearly. At time points (A) in figure 8, a single electron jumps onto the island. Since this is more likely for negative $\bar{x}$, due to the exponential dependance of E_L on position, we see a jump in the island's position towards the source contact located in the $-\bar{x}$ region. At time points (B), this electron now jumps off the island into the drain. Since again this is more likely closer to the drain due to the form of E_R, we see a quantum jump in the island's position to larger values of $+\bar{x}$. While the island is either empty/occupied, the non-Hermitian evolution suffered by the quantum trajectory causes the system to move towards the situation where the occupied/empty state becomes more and more probable. As a consequence of the exponential dependences of E_L and E_R, this means that the oscillations grow towards larger $+\bar{x}$, if the island is occupied, while they grow towards $-\bar{x}$, if the island is empty. The net effect is to pump the vibrational motion of the shuttle during the single trajectory and even though this growth is interspersed with dips due to the movement on or off of an electron. Once averaged over many quantum trajectories, the resulting effect is to pump the average energy of the oscillation in an unbounded manner (if there is no motional damping).

We now consider the full-blown quantum trajectory simulation of the system using the parameter values $\bar{\chi}_{ES} = 10$, $\bar{\kappa} = 2$, $\bar{\gamma}_L = 0.1$, $\bar{\gamma}_R = 0.8$, and $\lambda = \delta = 0.4$. We now have chosen a far larger value for the electrostatic force and are able to expand the Fock basis truncation to $N = 100$ using quantum trajectories. To determine the steady state quantum solution using a full matrix representation would now require over 26 GB of memory! The resulting simulation averages over 2000 quantum trajectories and required many days to execute on a 2 GHz Operton Dual processor 64-bit computer. In figure 9, we plot the right tunnel current $\langle \bar{i}_R \rangle$, as computed via quantum trajectories for the two endohedral spin states. We also plot the 'semiclassical'

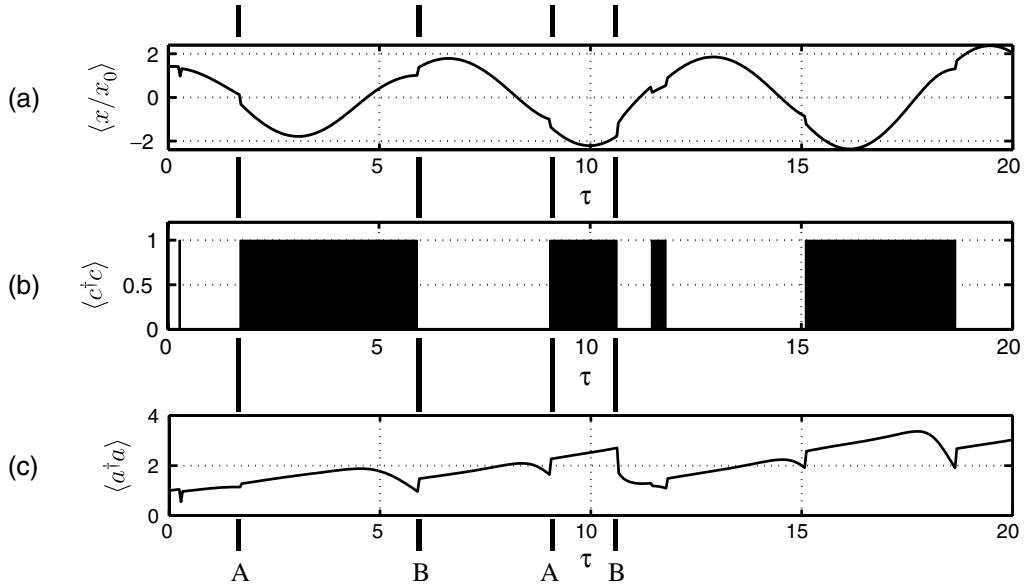

Figure 8. Quantum trajectories simulation (1 trajectory with a basis of 100 Fock states), of (41), for the case when $\bar{\gamma}_R = \bar{\gamma}_L = 1$, $\lambda = \delta = 0.4$, $\bar{\kappa} = \bar{n} = \delta = \eta = \bar{\chi}_{ES} = 0$. Graph (a) $\langle \bar{x}/x_0 \rangle = \langle \bar{x} \rangle$ versus τ, (b) $\langle c^\dagger c \rangle$, (c) $\langle a^\dagger a \rangle$. At times (A), a single electron jumps on to the island and as this is more likely towards negative $\bar{x}$, due to the exponential dependance of $E_L \sim e^{-\lambda \bar{x}}$ on position, we see a conditioned jump in the island's position towards $-\bar{x}$. At times (B), the electron jumps off the island into the drain and since this is more likely closer to the drain due to the form of $E_R \sim e^{+\lambda \bar{x}}$, we see a conditioned quantum jump towards $+\bar{x}$. While the island is either empty/occupied, the non-Hermitian evolution suffered by the quantum trajectory causes the system to move towards the occupied/empty state. The net effect is to pump the vibrational motion of the shuttle during interspersed jumps due to electrons arriving or leaving the island. Once averaged over many quantum trajectories, the resulting effect is to pump the average energy of the oscillation in an unbounded manner (if there is no motional damping).

dynamical evolution and the steady-state quantum expectation values for the currents where the latter is computed at the necessarily lower Fock truncation of $N = 40$. We can clearly see that the (incredibly computationally expensive) quantum trajectory simulation remarkably agrees very well with the values obtained from the steady-state numerics. It is not possible to plot out the Wigner function from the quantum trajectory simulation as this method can only yield the values of a small number of expectation values without running into the difficulty of requiring huge amounts of storage. However, the results shown in figure 9, strongly indicates that the technique of directly determining the quantum steady-state via the eigenvector of the Liouvillian matrix with vanishing eigenvalue, can extend to very large values of the electrostatic driving force $\bar{\chi}_{ES}$, without any significant lack of precision. As the physically relevant regime for $\bar{\chi}_{ES} \sim 20$, the

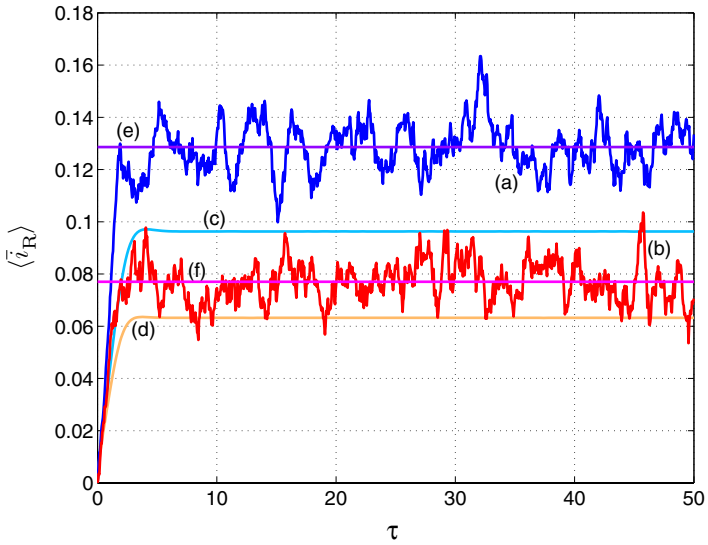

Figure 9. Graphs of the right tunnel current given as a function of rescaled time τ, for the two spin-states ($\pm\delta$). Graphs (a–b) (blue–red) are $\langle \bar{i}_R \rangle$ computed via a quantum trajectories solution of (41), for spin up/down (2000 trajectories). Graphs (c–d) (turquoise–orange) are the re-plotted 'semiclassical' solutions for the two cases of the shuttle spin state. Graphs (e–f) (magenta–purple) are $\langle \bar{i}_R \rangle$ computed via the steady-state solution for (41), on a $N = 40$, Fock basis representation. Again we have set $\bar{\kappa} = 2$, $\bar{\chi}_{ES} = 10$, $\gamma_L = 0.1$, $\gamma_R = 0.8$, $\lambda = \delta = 0.4$. This large numerical computation strongly confirms the validity of the smaller, less precise, steady-state full quantum simulation. In addition, we seem to see some time-dependant structure of the currents which should damp out with large τ.

behaviours we obtain here with $\bar{\chi}_{ES} \sim 3$–10, should therefore also hold in the physically relevant regime.

9.4. Estimating the steady-state quantum current noise

There are a number of methods to deduce the noise power spectral density $S(\omega)$. We will use the methods outlined in [64].

We first represent the instantaneous right tunnel current as $i_R(t) = e\,dN/dt$, where $dN(t)$, is a classical point process which represents the number (either zero or one) of tunnelling events seen in an infinitesmal time, dt, and e is the electric charge. We can consider $dN(t)$ to be the increment in the number of electrons $N(t)$, in the drain electrode in a time dt. The steady-state current is computed by $i_R^\infty = E[i(t)]_\infty$, where $E[\,\cdot\,]$ represents an average over the stochastic process describing the tunnelling events. In our case this is given by,

$$i_R^\infty = \gamma_R \langle \mathcal{J}[c e^{+\bar{\lambda}x}]\rho_\infty \rangle, \tag{60}$$

where the jump superoperator $\mathcal{J}[A]B \equiv ABA^{\dagger}$. The fluctuations in the current are quantified by the two-time correlation function

$$G(\tilde{t}) \equiv \mathrm{E}[i_{\mathrm{R}}(t)i_{\mathrm{R}}(t+\tilde{t}) - i_{\mathrm{R}}^{\infty\,2}]_{\infty} = ei_{\mathrm{R}}^{\infty}\delta(\tilde{t}) + \langle i_{\mathrm{R}}(t)i_{\mathrm{R}}(t+\tilde{t})\rangle_{\infty}^{\tilde{t}\neq 0}. \tag{61}$$

From the theory of open quantum systems [57], one can show that

$$G(\tilde{t}) = ei_{\mathrm{R}}^{\infty}\delta(\tilde{t}) + e^2\{\mathrm{Tr}[\mathcal{J}_{\mathrm{R}}\mathrm{e}^{\mathcal{L}\tilde{t}}\mathcal{J}_{\mathrm{R}}\rho_{\infty}] - \mathrm{Tr}[\mathcal{J}_{\mathrm{R}}\rho_{\infty}]^2\}_{\tilde{t}\neq 0}^{\infty}, \tag{62}$$

where $\mathcal{J}_{\mathrm{R}} = \sqrt{\gamma_{\mathrm{R}}}\,c\,\exp(-\bar{\lambda}x)$ (see (21)), and the Liouvilian evolution, $\exp(\mathcal{L}\tilde{t})$, is according to the master equation (41). In the case of a decoupled system ($\lambda = 0$), this leads to a normally ordered correlation function while one obtains an antinormally ordered correlation function if one were studying the noise of the left tunnel current [70]. For the coupled system the interpretation of the operator ordering is more complicated.

The current noise spectral density is given by[6]

$$S(\omega) \equiv 2\int_{-\infty}^{+\infty} \mathrm{d}\tilde{t}G(\tilde{t})\mathrm{e}^{\mathrm{i}\omega\tilde{t}}. \tag{63}$$

In terms of our rescaled variables and parameters, $\tau = \omega_0 t$, and (46), we set $\tilde{\tau} = \omega_0\tilde{t}$, to obtain,

$$G(\tilde{\tau}) = ei_{\mathrm{R}}^{\infty}\delta(\tilde{\tau})\omega_0 + e^2\omega_0^2\bar{\gamma}_{\mathrm{R}}^2\{\mathrm{Tr}[\mathcal{J}[c\mathrm{e}^{+\lambda\bar{x}}]\mathrm{e}^{\mathcal{L}\tilde{t}}\mathcal{J}[+c\mathrm{e}^{+\lambda\bar{x}}]\rho_{\infty}] - \mathrm{Tr}[\mathcal{J}[c\mathrm{e}^{+\lambda\bar{x}}]\rho_{\infty}]^2\}_{\tilde{\tau}\neq 0}^{\infty}, \tag{64}$$

where now the Liouvillian evolution is given by (51). The spectral density is now given by

$$S(\omega/\omega_0) = 2ei_{\mathrm{R}}^{\infty} + e^2\omega_0\bar{\gamma}_{\mathrm{R}}^2\int_{-\infty}^{+\infty}\mathrm{e}^{\mathrm{i}(\omega/\omega_0)\tilde{\tau}}\,\mathrm{d}\tilde{\tau}\{\mathrm{Tr}[\mathcal{J}[c\mathrm{e}^{+\lambda\bar{x}}]\mathrm{e}^{\mathcal{L}\tilde{t}}\mathcal{J}[c\mathrm{e}^{+\lambda\bar{x}}]\rho_{\infty}] - \mathrm{Tr}[\mathcal{J}[c\mathrm{e}^{+\lambda\bar{x}}]\rho_{\infty}]^2\}_{\tilde{\tau}\neq 0}^{\infty}. \tag{65}$$

From this we can derive the Fano factor, $F = S(\omega)/(2ei_{\mathrm{R}}^{\infty})$, to be

$$F(\omega/\omega_0) = 1 + \frac{\bar{\gamma}_{\mathrm{R}}^2}{2i_{\mathrm{R}}^{\infty}}\int_{-\infty}^{+\infty}\mathrm{e}^{\mathrm{i}(\omega/\omega_0)\tilde{\tau}}\mathrm{d}\tilde{\tau}\{\mathrm{Tr}[\mathcal{J}[c\mathrm{e}^{+\lambda\bar{x}}]\mathrm{e}^{\mathcal{L}\tilde{t}}\mathcal{J}[c\mathrm{e}^{+\lambda\bar{x}}]\rho_{\infty}] - \mathrm{Tr}[\mathcal{J}[c\mathrm{e}^{+\lambda\bar{x}}]\rho_{\infty}]^2\}_{\tilde{\tau}\neq 0}^{\infty}. \tag{66}$$

The Fano factor F gives information on the statistics of the tunnel current noise. If $F = 1$ then the noise is completely uncorrelated/Poissonian, i.e. white noise. If $F > 1$, then the noise is known as super-Poissonian and the tunnel events are bunched. If $F < 1$, then the noise is known as sub-Poissonian and the tunnelling events are anti-bunched, i.e. there is little chance that a second tunnel event will closely follow a previous event. Quantum correlations within the coupled system are primarily responsible for $F \neq 0$.

[6] As noted in [71], the spectral power density of relevance depends on the characteristics of the measurement scheme used to detect the current noise fluctuations. In the case of a purely passive detector scheme (where the detector can only be excited by the current fluctuations and cannot itself excite any fluctuations in the current), the detected current correlations $\langle i_{\mathrm{R}}(t)i_{\mathrm{R}}(t+\tau)\rangle$ ($\langle i_{\mathrm{R}}(t+\tau)i_{\mathrm{R}}(t)\rangle$), yields either the power density only at positive(negative) frequencies. Our non-symmetrized definition of the spectral power density corresponds to recent experimental uses where our $S(\omega)$, with $\omega > 0$, corresponds to $S_f(+\omega)$ in [72] and [73]. With this convention $\omega > 0$ in all our formulae for spectral densities, Fano functions etc.

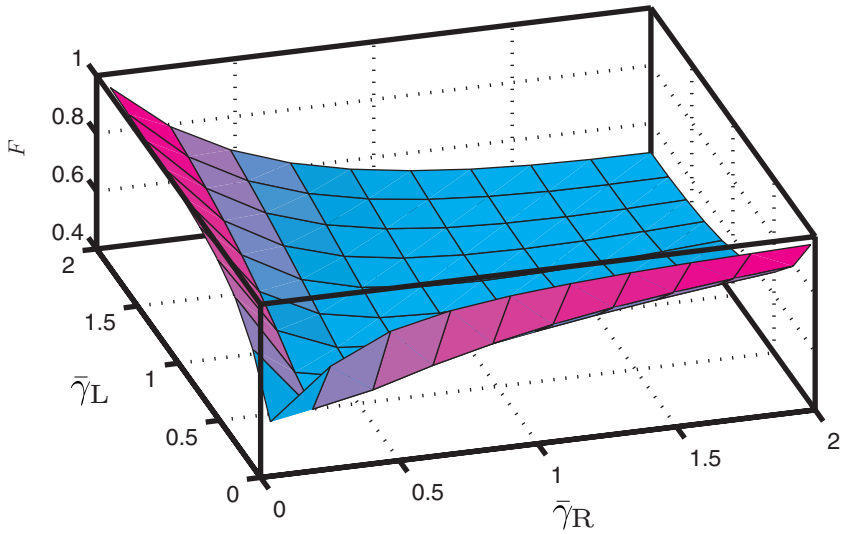

Figure 10. Graph of Fano function F, for the decoupled system $\lambda = 0$, $\bar{\kappa} = 0.1$, $\bar{\chi}_{ES} = 0$. Numerical results agree with the analytical formula for a sequential double tunnel barrier device $F = (\bar{\gamma}_L^2 + \bar{\gamma}_R^2)/(\bar{\gamma}_L + \bar{\gamma}_R)^2$ (see equation (67)).

Using numerical tools developed in quantum optics [59], we can compute $F(\omega/\omega_0)$. To demonstrate its use, we compare in figure 10 the results calculated using the numerical tools for the decoupled electronic-vibrational system (by setting $\lambda = 0$), with the standard results for a two-state sequential tunnelling process [48, 49],

$$\bar{i}_R^{\infty} = \frac{\bar{\gamma}_L \bar{\gamma}_R}{\bar{\gamma}_L + \bar{\gamma}_R}, \qquad F = \frac{\bar{\gamma}_L^2 + \bar{\gamma}_R^2}{(\bar{\gamma}_L + \bar{\gamma}_R)^2}. \tag{67}$$

The numerical results shown in figure 10 are in agreement with the analytical formula of equation (67). In figure 11, we display the current noise spectra for various frequencies, i.e.

$$F(\omega/\omega_0) = 1 - \frac{|S(\omega/\omega_0)|}{2ei_R^{\infty}}, \tag{68}$$

and see that typically the noise is sub-Poissonian. In figure 12, we contour plot the DC (or zero frequency), Fano factors for the decoupled and coupled system and observe that the coupled system displays stronger anti-bunching when $\bar{\gamma}_L \sim \bar{\gamma}_R$, than in the decoupled case. However in the parameter region where we are interested, $\bar{\gamma}_R \gg \bar{\gamma}_L$, the DC Fano factors of the decoupled and coupled system are very similar.

9.5. Measurement time

The final quantity we must determine, given the DC current signals and current noise associated with the two endohedral spin-states, is the measurement time τ_m, required to differentiate the two currents $\bar{i}_R^{\uparrow\infty}$ and $\bar{i}_R^{\downarrow\infty}$. This is given by the expression [62],

$$\tau_m = \frac{(\sqrt{S_1} + \sqrt{S_2})^2}{2(\Delta I)^2}, \tag{69}$$

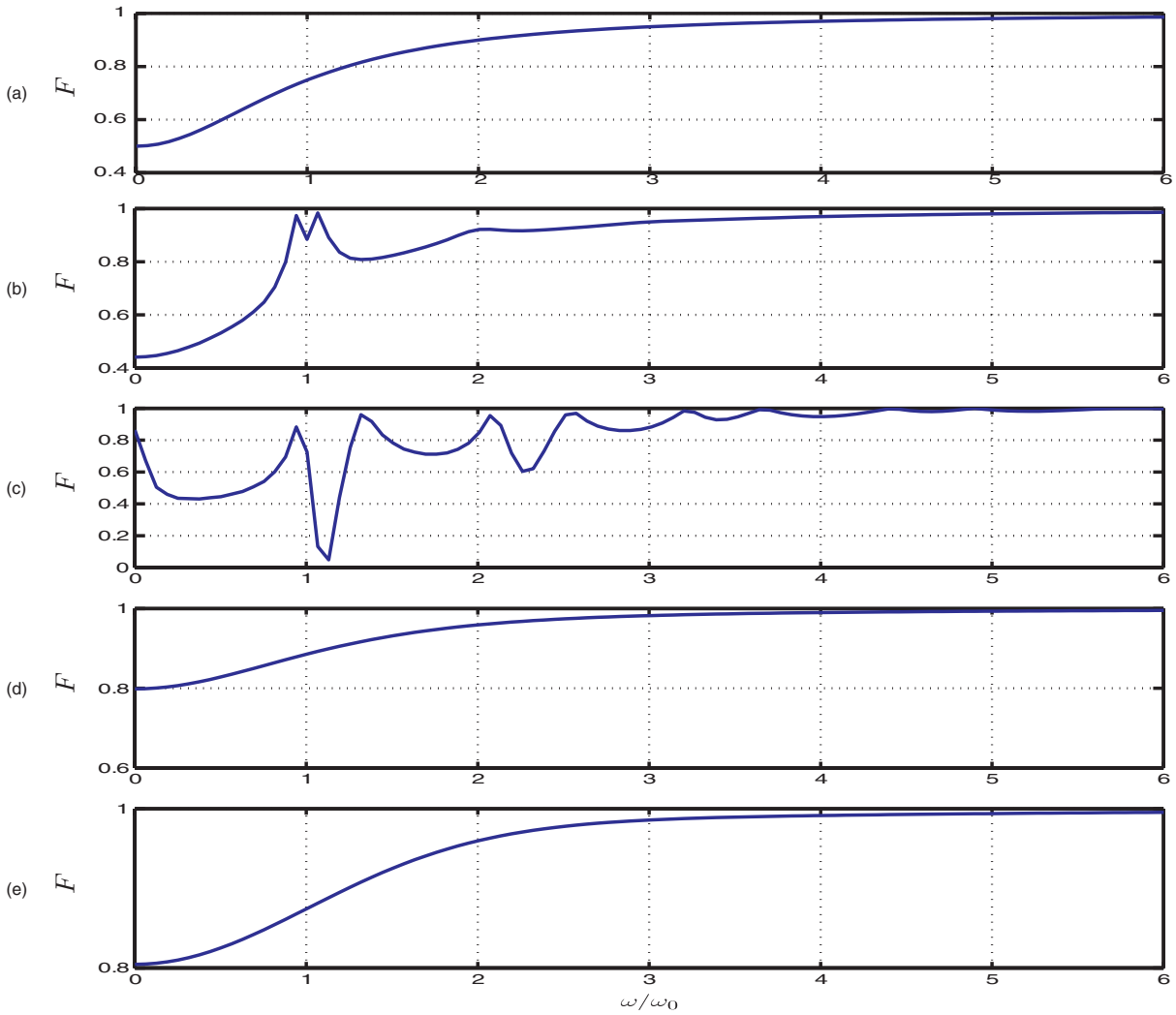

Figure 11. Frequency dependance of the numerically evaluated Fano function (66), for various parameter values (a) $\bar{\kappa} = 0.05$, $\bar{\chi}_{ES} = 0$, $\bar{\gamma}_L = \bar{\gamma}_R = 0.5$ and $\lambda = 0$, (b) $\lambda = 0.4$, $\bar{\kappa} = 0.1$, $\bar{\chi}_{ES} = 0$, $\bar{\gamma}_L = \bar{\gamma}_R = 0.5$, (c) $\lambda = 0.4$, $\bar{\kappa} = 0.1$, $\bar{\chi}_{ES} = 3$, $\bar{\gamma}_L = 0.1$, $\bar{\gamma}_R = 0.9$, (d) $\lambda = 0.4$, $\bar{\kappa} = 3$, $\bar{\chi}_{ES} = 3$, $\bar{\gamma}_L = 0.1$, $\bar{\gamma}_R = 0.9$, (e) $\lambda = 0.4$, $\bar{\kappa} = 3$, $\bar{\chi}_{ES} = 10$, $\bar{\gamma}_L = 0.1$, $\bar{\gamma}_R = 0.9$.

where S_1, and S_2, are the DC current noise spectral densities for the two cases of spin up/down while $\Delta I \equiv |\langle \bar{i}_R^{\uparrow\infty} \rangle - \langle \bar{i}_R^{\downarrow\infty} \rangle|$. In figure 13, we plot $\log_{10} \tau_m$, for various $\bar{\gamma}_L$, $\bar{\gamma}_R$. We see clearly that when $\bar{\gamma}_R \sim \bar{\gamma}_L$, τ_m must be very large to discriminate between the very small difference in steady-state currents. In the parameter regions, we are concerned with, i.e. $\bar{\gamma}_R/\bar{\gamma}_L \gg 1$, this measurement time is $\tau_m \sim 10^1$–10^2, in the natural units of the oscillator ($\omega_0 = 2\pi \times 1\,\text{GHz}$), or a few tens of nanoseconds. Thus in this parameter region, the measurement time is very realistic.

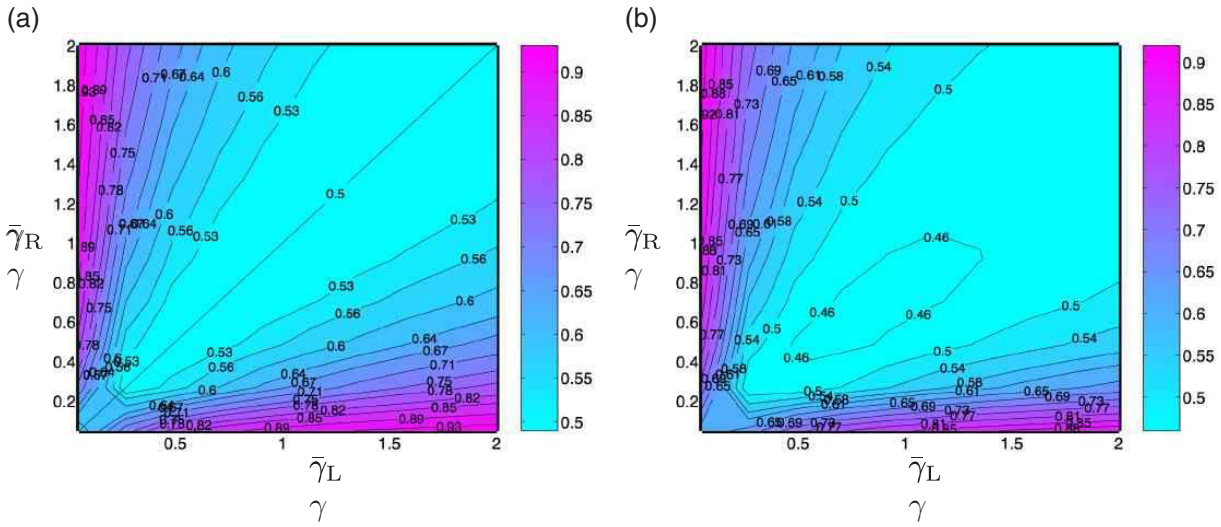

Figure 12. Contour plots of the numerically computed DC Fano factor $F(\omega/\omega_0 = 0)$, (66), for the (a) decoupled system with $\bar{\chi}_{ES} = 0$, $\bar{\kappa} = 0.1$, and (b) the coupled system with $\lambda = 0.4$, $\bar{\chi}_{ES} = 3$, $\bar{\kappa} = 3$. In (b) we can see the coupling between the electronic and vibrational systems influencing the DC quantum noise. The anisotropy towards $\bar{\gamma}_L$, is due to the overall anisotropy of the current flow due to the applied bias.

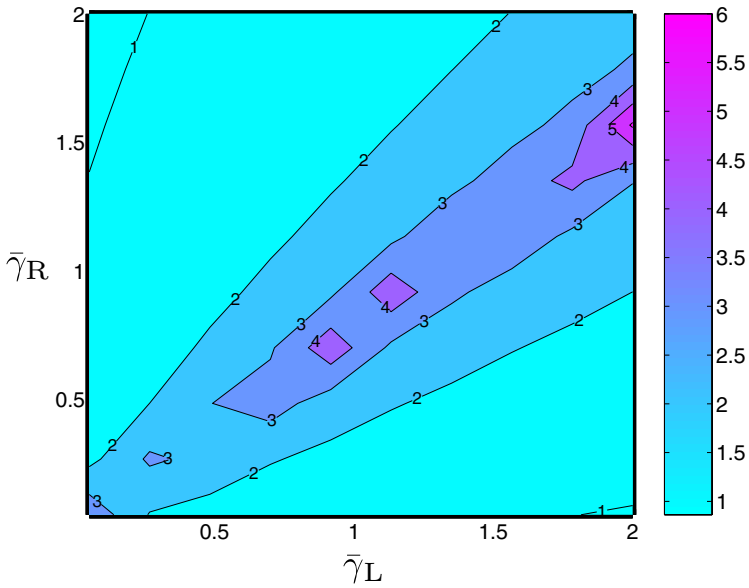

Figure 13. Contour plot of the $\log_{10}(\tau_m)$, of the measurement time from equation (69), required to distinguish the two spin states from the current for the coupled system with $\lambda = \delta = 0.4$, $\bar{\chi}_{ES} = 3$, $\bar{\kappa} = 3$.

10. Summary

In summary, we have shown that the right-hand tunnel current of a strongly damped single electron shuttle operating in the Coulomb blockade regime has very high sensitivity to small equilibrium position displacements of the shuttle. We considered a $N@C_{60}$ molecular shuttle whose endohedral spin can exert a force on the molecule when placed in a large magnetic field gradient. By placing a large nanoscopic magnet nearby, a tiny $\sim \pm 10^{-15}$ N force is suffered by the molecular island arising from the endohedral spin state $S_z = \pm 3/2$. This small force alters the equilibrium position of the island in the presence of the electrostatic driving force, motional damping, and harmonic restoring force. Through the extremely sensitive (exponential), dependence of the conductance on the tunnel separations, the shift in the equilibrium position of the island profoundly influences the current flow. We determined the current noise spectral density and the measurement time required to distinguish between the two DC steady-state current signals (spin up and down), in the presence of steady-state quantum noise.

The results we have found would strongly indicate that there are realistic parameter regimes where the spin state-dependent currents are distinguishable within several tens of nanoseconds. Thus this device should thus be capable of spin-detection. Alternatively, similar devices (without an endohedral spin) should be capable of discriminating small, $\sim \pm 10^{-15}$ N, static forces on a C_{60} island.

Acknowledgments

This work was supported via an EC 5FP FET QIPC Project QIPDDF-ROSES. H-SG acknowledges the support from the National Science Council, Taiwan under contract no NSC 94-2112-M-002-028.

References

[1] Rugar H J M D, Budakian R and Chui B W 2004 *Nature* **430** 329
[2] Xiao M, Martin I, Yablonovitch E and Jiang H W 2004 *Nature* **430** 435
[3] Elzerman J M, Hanson R, van Beveren L H W, Witkamp B, Vandersypen L M K and Kouwenhoven L P 2004 *Nature* **430** 431
[4] Gorelik L Y, Isacsson A, Voinova M V, Kasemo B, Shekhter R I and Jonson M 1998 *Phys. Rev. Lett.* **80** 4526
[5] Isacsson A 2001 *Phys. Rev.* B **6403** 035326
[6] Fedorets D, Gorelik L Y, Shekhter R I and Jonson M 2002 *Europhys. Lett.* **58** 99
[7] Shekhter R I, Galperin Y, Gorelik L Y, Isacsson A and Jonson M 2003 *J. Phys.: Condens. Matter* **15** R441
[8] Boese D and Schoeller H 2001 *Europhys. Lett.* **54** 668
[9] McCarthy K D, Prokof'ev N and Tuominen M T 2003 *Phys. Rev.* B **67** 245415
[10] Flensberg K 2003 *Phys. Rev.* B **68** 205323
[11] Braig S and Flensberg K 2003 *Phys. Rev.* B **68** 205324
[12] Chtchelkatchev N M, Belzig W and Bruder C 2004 *Phys. Rev.* B **70** 193305
[13] Isacsson A and Nord T 2004 *Europhys. Lett.* **66** 708
[14] Mitra A, Aleiner I and Millis A J 2004 *Phys. Rev.* B **69** 245302
[15] Pistolesi F 2004 *Phys. Rev.* B **69** 245409
[16] Blanter Y M, Usmani O and Nazarov Y V 2004 *Phys. Rev. Lett.* **93** 136802
[17] Blencowe M P and Wybourne M N 2000 *Appl. Phys. Lett.* **77** 3845
[18] Armour A D, Blencowe M P and Zhang Y 2004 *Phys. Rev.* B **69** 125313

[19] Armour A D 2004 *Phys. Rev.* B **70** 165315
[20] Blencowe M 2004 *Phys. Rep.* **395** 159
[21] Park H, Park J, Lim A K L, Anderson E H, Alivisatos A P and McEuen P L 2000 *Nature* **407** 57
[22] Erbe A, Weiss C, Zwerger W and Blick R H 2001 *Phys. Rev. Lett.* **8709** 096106
[23] Scheible D V, Erbe A and Blick R H 2002 *New J. Phys.* **4** 86
[24] Scheible D V and Blick R H 2004 *Appl. Phys. Lett.* **84** 4632
[25] Knobel R G and Cleland A N 2003 *Nature* **424** 291
[26] LaHaye M D, Buu O, Camarota B and Schwab K C 2004 *Science* **304** 74
[27] Novotny T, Donarini A and Jauho A P 2003 *Phys. Rev. Lett.* **90** 256801
[28] Fedorets D 2003 *Phys. Rev.* B **68** 033106
[29] Fedorets D, Gorelik L Y, Shekhter R I and Jonson M 2004 *Phys. Rev. Lett.* **92** 166801
[30] Smirnov A Y, Mourokh L G and Horing N J M 2004 *Phys. Rev.* B **69** 155310
[31] Mozyrsky D, Martin I and Hastings M B 2004 *Phys. Rev. Lett.* **92** 018303
[32] Utami D W, Goan H-S and Milburn G J 2004 *Phys. Rev.* B **70** 075303
[33] Rodrigues D A and Armour A D 2005 *New J. Phys.* **7** 251
[34] Novotny T, Donarini A, Flindt C and Jauho A P 2004 *Phys. Rev. Lett.* **92** 248302
[35] Donarini A 2004 *PhD Thesis* MIC, Technical University of Denmark
[36] Flindt C, Novotny T and Jauho A-P 2005 *Europhys. Lett.* **69** 475
[37] MacKinnon A and Armour A D 2003 *Physica* E **18** 95
[38] Donarini A, Novotny T and Jauho A P 2004 *Semicond. Sci. Technol.* **19** S430
[39] Flindt C, Novotny T and Jauho A P 2004 *Phys. Rev.* B **70** 205334
[40] Twamley J 2003 *Phys. Rev.* A **67** 052318
[41] Huang X M H, Zorman C A, Mehregany M and Roukes M L 2003 *Nature* **421** 496
[42] Feng M and Twamley J 2004 *Phys. Rev.* A **70** 030303
[43] Pasupathy A N, Bialczak R C, Martinek J, Grose J E, Donev L A K, McEuen P L and Ralph D C 2004 *Science* **306** 86
[44] Gorelik L Y, Kulinich S I, Shekhter R I, Jonson M and Vinokur V M 2005 *Phys. Rev.* B **71** 035327
[45] Gorelik L Y, Kulinich S I, Shekhter R I, Jonson M and Vinokur V M 2005 *Phys. Rev. Lett.* **95** 116806
[46] Fedorets D, Gorelik L Y, Shekhter R I and Jonson M 2005 *Phys. Rev. Lett.* **95** 057203
[47] Gorelik L Y, Fedorets D, Shekhter R I and Jonson M 2005 *New J. Phys.* **7** 242
[48] Blanter Y M and Buttiker M 2000 *Phys. Rep.* **336** 2
[49] Davies J H, Hyldgaard P, Hershfield S and Wilkins J W 1992 *Phys. Rev.* B **46** 9620
[50] Berman G P, Doolen G D, Hammel P C and Tsifrinovich V I 2000 *Phys. Rev.* B **61** 14694
[51] Utami D W, Goan H-S, Holmes C A and Milburn G J 2005 *Preprint* cond-mat/059748
[52] Dalibard J, Castin Y and Molmer K 1992 *Phys. Rev. Lett.* **68** 580
[53] Gisin N and Percival I C 1992 *J. Phys. A: Math. Gen.* **25** 5677
[54] Gisin N and Percival I C 1993 *J. Phys. A: Math. Gen.* **26** 2233
[55] Gisin N and Percival I C 1993 *J. Phys. A: Math. Gen.* **26** 2245
[56] Wiseman H M and Milburn G J 1993 *Phys. Rev.* A **47** 1652
[57] Carmichael H 1993 *An Open Systems Approach to Quantum Optics* (Berlin: Springer)
[58] Carmichael H J 1996 *Quantum Semiclass. Opt.* **8** 47 special issue on stochastic quantum optics
[59] Tan S, http://www.phy.auckland.ac.nz/Staff/smt/qtoolbox/download
[60] Gardiner C W and Zoller P 2000 *Quantum Noise* 2nd edn (Berlin: Springer)
[61] Korotkov A N 1999 *Phys. Rev.* B **60** 5737
[62] Korotkov A N 2001 *Phys. Rev.* B **63** 115403
[63] Goan H-S, Milburn G J, Wiseman H M and Sun H B 2001 *Phys. Rev.* B **63** 125326
[64] Goan H-S and Milburn G J 2001 *Phys. Rev.* B **64** 235307 appendix

[65] Goan H-S 2003 *Quantum Inform. Comput.* **3** 121
[66] Goan H-S 2004 *Phys. Rev.* B **70** 075305
[67] Schaefers H and Strunz W T 2005 *Phys. Rev.* B **71** 075321
[68] Golub G and Loan C V 1996 *Matrix Computations* (Baltimore, MD: Johns Hopkins University Press)
[69] Flindt C 2005 *PhD Thesis* MSc Department of Micro and Nanotechnology, Technical University of Denmark, http://www.mic.dtu.dk
[70] Milburn G J, Sun H B and Upcroft B 2000 *Aust. J. Phys.* **53** 463
[71] Lebedev A V, Crépieux A and Martin T 2005 *Phys. Rev.* B **71** 075416
[72] Schoelkopf R, Clerk A A, Girvin S, Lehnert K and Devoret M 2002 *Preprint* cond-mat/0210247
[73] Deblock R, Onac E, Gurevich L and Kouwenhoven L P 2003 *Science* **301** 203